Uplink Joint Positioning and Synchronization in Cell-Free Deployments with Radio Stripes

Alessio Fascista*, Benjamin J. B. Deutschmann†, Musa Furkan Keskin‡, Thomas Wilding†,
Angelo Coluccia*, Klaus Witrisal†, Erik Leitinger†, Gonzalo Seco-Granados§, Henk Wymeersch‡
*Università del Salento, Italy, †Graz University of Technology, Austria,
‡Chalmers University of Technology, Sweden, §Universitat Autonoma de Barcelona, Spain

2023 IEEE International Conference on Communications Workshops (ICC Workshops) | 979-8-3503-3307-7/23/$31.00 ©2023 IEEE | DOI: 10.1109/ICCWORKSHOPS57953.2023.10283650

***Abstract*—Radio stripes (RSs) is an emerging technology in beyond 5G and 6G wireless networks to support the deployment of cell-free architectures. In this paper, we investigate the potential use of RSs to enable joint positioning and synchronization in the uplink channel at sub-6 GHz bands. The considered scenario consists of a single-antenna user equipment (UE) that communicates with a network of multiple-antenna RSs distributed over a wide area. The UE is assumed to be unsynchronized to the RSs network, while individual RSs are time- and phase-synchronized. We formulate the problem of joint estimation of position, clock offset and phase offset of the UE and derive the corresponding maximum-likelihood (ML) estimator, both with and without exploiting carrier phase information. To gain fundamental insights into the achievable performance, we also conduct a Fisher information analysis and inspect the theoretical lower bounds numerically. Simulation results demonstrate that promising positioning and synchronization performance can be obtained in cell-free architectures supported by RSs, revealing at the same time the benefits of carrier phase exploitation through phase-synchronized RSs.**

***Index Terms*– Radio stripes, cell-free massive MIMO, positioning, synchronization, carrier phase, sub-6 GHz.**

I. Introduction

Cell-free massive multiple-input-multiple-output (MIMO) has recently emerged as a promising technology for beyond 5G wireless networks to overcome challenges associated with conventional network-centric implementations, such as inter-cell interference and large intra-cell variations in data rate [1]–[3]. In user-centric cell-free architectures, each user equipment (UE) communicates with a UE-specific subset of widely distributed access points (APs) that cooperatively serve it using phase-synchronized transmission/reception enabled by fronthaul links [2]. Such an architecture not only improves communication metrics (i.e., more uniform coverage and better interference management), but also brings significant benefits for positioning and sensing [4], [5], which is an opportunity for integrated sensing and communications (ISAC) in cell-free contexts [6]. In particular, phase-coherent processing with wide aperture enables exploitation of *wavefront curvature* effects (i.e., near-field) [4], [5] and high-resolution *carrier phase (CP)* information [7] to estimate UE/object positions. In cell-free scenarios, the near-field region can be expressed in terms of Fraunhofer distance, with the largest dimension of radiating elements linked to the maximum separation of APs.

Among cell-free implementation alternatives, the RSs technology holds great potential as a cost-efficient architecture for dense area deployments, such as stadiums and railway stations [3], [8]. RSs, also called RadioWeaves [9]–[11], consist of multiple antenna elements and processing units fitted inside the same cable, which can be easily deployed over a large area [3]. Serially connected RSs communicate with a central processing unit (CPU) via a shared bus that simultaneously provides synchronization and power supply [3]. Unlike stripe-like reconfigurable intelligent surfaces (RISs) [12], RSs can actively transmit and sample incoming signals in reception. From the viewpoint of positioning and sensing, synchronization of distributed arrays has been experimentally shown to improve angle-of-arrival (AoA) estimation accuracy [13]. Hence, synchronized and distributed RSs offer a viable cell-free solution to reap the benefits in positioning and sensing.

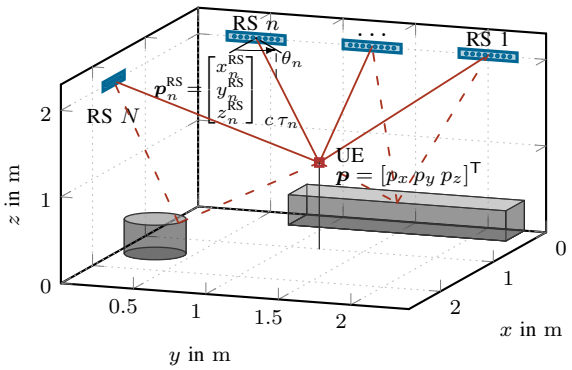

Fig. 1. General scenario of uplink UE positioning supported by a radio stripe (RS) network with N stripes.

Despite a considerable amount of research on the communications [8], [9], [11], [14], wireless power transfer [10], [15], and sensing [4], [5] aspects of RSs, no studies have investigated the potential of positioning aided by widely distributed RSs at sub-6 GHz bands. Recent work investigated coherent localization in distributed millimeter-wave (mmWave) massive MIMO systems [16]–[18]. However, two major differences exist between sub-6 GHz and mmWave operation. First, ensuring phase synchronization and calibration among distributed arrays at mmWave bands is extremely challenging since hardware imperfections (e.g., phase noise and frequency errors) become more severe as the carrier frequency increases [19, Sec. 6.2.1]. Second, unlike the sparse nature of mmWave propagation, sub-6 GHz channels involve dense multipath components (DMCs) [10], [20] that should be incorporated into signal modeling as a disturbance with certain statistical characterization. Therefore, the question remains unanswered as to *under what conditions and to what extent phase synchronization and accompanying phase-coherent processing can improve positioning in a widely distributed RSs network at sub-6 GHz*. To fill this knowledge gap, this paper addresses the problem of uplink positioning

and synchronization of a UE supported by a network of RSs geographically distributed over a large area in a cell-free deployment scenario. In contrast to co-located massive MIMO based localization (e.g., [21]), distributed MIMO setups with phase-coherent processing enable exploitation of spherical wavefront through near-field conditions and CP information to obtain high-resolution location estimates. The main contributions of the paper are as follows:

(i) We investigate the problem of uplink joint positioning and synchronization of a UE with distributed RSs, considering the distinctive properties of sub-6 GHz operation, including phase and time synchronization capability [22], dense multipath environment [10] and CP exploitation.

(ii) We derive the maximum likelihood (ML) estimators and the corresponding Cramér-Rao lower bounds (CRLBs) on position, clock and phase offset estimation, both with and without exploiting CP information.

(iii) We carry out extensive simulation analysis to showcase the impact of various system parameters (i.e., bandwidth, aperture size, signal-to-dense multipath-plus-noise ratio (SDNR), presence/absence of phase synchronization) on positioning and clock offset estimation accuracy, offering valuable insights into practical RS deployments towards 6G networks.

Notations: $\mathrm{Toep}(\boldsymbol{x}, \boldsymbol{x}^{\mathsf{H}})$ denotes a Hermitian Toeplitz matrix with first column $\boldsymbol{x}$ and first row $\boldsymbol{x}^{\mathsf{H}}$. $\mathrm{reshape}_{M,K}(\cdot)$ reshapes a vector into an $M \times K$ matrix. $[\boldsymbol{x}]_i$ denotes the i-th element of the vector $\boldsymbol{x}$ and $[\boldsymbol{X}]_{i,j}$ the element of row i and column j of the matrix $\boldsymbol{X}$. The vector $\mathbf{1}_n$ is 1 at the n-th entry and 0 elsewhere. $\Re\{x\}$ denotes the real part of x.

II. System Model and Problem Formulation

In this section, we describe the uplink positioning scenario with RSs acting as receivers and a single UE in the role of transmitter, illustrate the signal model at the RSs and formulate the joint positioning and synchronization problem.

A. Uplink Positioning Scenario with Radio Stripes

Consider a single-input-multiple-output (SIMO) system with a RSs network composed of N stripes, each consisting of M antennas, and a single UE equipped with a single antenna and communicating with the network through the uplink (UL) channel [8], [15]. The RSs network is assumed to have perfect *phase synchronization* among individual stripes, thereby effectively turning it into a large multiple-antenna access point [3, Sec. 3.1], while the UE has unknown *phase offset* δ_ϕ and unknown *clock offset* δ_τ with respect to the RSs network. The wavefront of the signal transmitted by the UE is assumed planar over each individual RS (i.e., individual RSs lie in the far-field of the UE), but no longer planar over the RSs network seen as a whole due to a large aperture distributed over a wide area. The RSs are deployed around a rectangle located at a specific height from the floor level, as depicted in Fig. 1. Each individual RS is placed at a known position $\boldsymbol{p}_n^{\text{RS}} = [x_n^{\text{RS}}\ y_n^{\text{RS}}\ z_n^{\text{RS}}]^{\mathsf{T}}$ with known orientation β_n around the z-axis, measured counter-clockwise from the x-axis[1], while the UE is located at an unknown position $\boldsymbol{p} = [p_x\ p_y\ p_z]^{\mathsf{T}}$.

[1]The orientation of each RS is defined by a single rotation around the z-axis, meaning that the RSs are completely aligned along the $x-y$ plane.

B. Signal and Channel Models

For UL communications, the UE transmits orthogonal frequency division multiplexing (OFDM) pilots $\boldsymbol{s} = [s_0\ \cdots\ s_{K-1}]^{\mathsf{T}} \in \mathbb{C}^{K\times 1}$ over K subcarriers with subcarrier spacing Δ_f, e.g., sounding reference signal (SRS) for 5G new radio (NR) UL positioning [23]. Assuming a quasi-static block fading condition, the UL received signal at the n-th RS over subcarrier k can be written as [10], [21]

$$\boldsymbol{y}_{n,k} = \boldsymbol{h}_{n,k} s_k + \boldsymbol{w}_{n,k}^{\text{DMC}} s_k + \boldsymbol{z}_{n,k} \in \mathbb{C}^{M\times 1}\ , \tag{1}$$

where $\boldsymbol{h}_{n,k} \in \mathbb{C}^{M\times 1}$ denotes the deterministic channel components including the line-of-sight (LoS) path and the possible non-line-of-sight (NLoS) contributions originating from dominant reflections from large objects, $\boldsymbol{w}_{n,k}^{\text{DMC}} \in \mathbb{C}^{M\times 1}$ represents the contribution from DMCs, and $\boldsymbol{z}_{n,k} \in \mathbb{C}^{M\times 1}$ denotes circularly symmetric complex Gaussian noise with $\boldsymbol{z}_{n,k} \sim \mathcal{CN}(\mathbf{0}_M, \sigma^2 \mathbf{I}_M)$, with σ^2 denoting the noise power. In this work, we consider the simplified scenario in which the LoS path over each UE-RS link is assumed to be dominant compared to the additional NLoS paths, giving rise to the following geometric channel model [10], [15], [21]

$$\boldsymbol{h}_{n,k} = \alpha_n e^{j\phi_n} \boldsymbol{a}(\theta_n) e^{-j2\pi k \Delta_f \widetilde{\tau}_n}\ , \tag{2}$$

where $\alpha_n \in \mathbb{R}$ is the large-scale fading amplitude coefficient, ϕ_n is the phase term involving the effects of one-way signal propagation (related to the UE position $\boldsymbol{p}$) and phase offset between the RSs network and UE, given by

$$\phi_n = -2\pi f_c \tau_n + \delta_\phi, \tag{3}$$

$$\tau_n = \frac{1}{c}\|\boldsymbol{p} - \boldsymbol{p}_n^{\text{RS}}\|, \tag{4}$$

$\widetilde{\tau}_n$ is the pseudo-delay including the effect of one-way propagation and the clock offset of the UE, namely

$$\widetilde{\tau}_n = \tau_n + \delta_\tau, \tag{5}$$

$\boldsymbol{a}(\theta_n) \in \mathbb{C}^{M\times 1}$ is the RS array response to a signal impinging with AoA θ_n (azimuth angle relative to the boresight of the n-th RS antenna array). Without loss of generality, we assume for each RS a uniform linear array (ULA) with element spacing[2] d, so that the array response vector takes the form $\boldsymbol{a}(\theta) \triangleq \left[e^{-j\frac{2\pi}{\lambda}d\left(\frac{M-1}{2}\right)\sin\theta}\ \cdots\ e^{j\frac{2\pi}{\lambda}d\left(\frac{M-1}{2}\right)\sin\theta}\right]^{\mathsf{T}}$ with $\lambda = c/f_c$, f_c and c denoting the wavelength, carrier frequency and speed of propagation, respectively. The AoA θ_n relates the known position and orientation of the n-th RS and the unknown UE position according to

$$\theta_n = \frac{\pi}{2} - \mathrm{atan2}\left([\boldsymbol{p}_n']_2, [\boldsymbol{p}_n']_1\right)\ , \tag{6}$$

where $\mathrm{atan2}(y,x)$ is the four-quadrant inverse tangent and

$$\boldsymbol{p}_n' = \boldsymbol{M}^{-1}(\beta_n)(\boldsymbol{p} - \boldsymbol{p}_n^{\text{RS}}) \tag{7}$$

is the UE position in the local reference frame of the n-th RS, and $\boldsymbol{M}(\beta)$ is the rotation matrix around the z-axis.

C. Dense Multipath Components

The dense multipath term in (1) can be modeled as a stochastic component with distribution [21], [25]

$$\boldsymbol{w}_n^{\text{DMC}} \sim \mathcal{CN}(\mathbf{0}_{MK}, \boldsymbol{R}^{\text{DMC}}(\boldsymbol{\eta}_{\text{DMC}}))\ , \tag{8}$$

[2]For RS deployments, the element spacing can be larger than the standard half-wavelength spacing to increase spatial resolution [11], [24, Ch. 2.2.4].

with $\boldsymbol{w}_n^{\text{DMC}} \triangleq [(\boldsymbol{w}_{n,0}^{\text{DMC}})^{\mathsf{T}} \ \cdots \ (\boldsymbol{w}_{n,K-1}^{\text{DMC}})^{\mathsf{T}}]^{\mathsf{T}} \in \mathbb{C}^{MK\times 1}$ denotes the DMC observed in the spatial-frequency domain, and $\boldsymbol{R}^{\text{DMC}} \in \mathbb{C}^{MK\times MK}$ is the spatial-frequency covariance matrix of the DMC. Assuming spatially white DMC and the Kronecker separability of the spatial and frequency domains (i.e., uncorrelated scattering between angle and delay domains), $\boldsymbol{R}^{\text{DMC}}$ can be written as [20, Eq. (2.69)], [21], [25]

$$\boldsymbol{R}^{\text{DMC}}(\boldsymbol{\eta}_{\text{DMC}}) = \boldsymbol{R}_f(\boldsymbol{\eta}_{\text{DMC}}) \otimes \mathbf{I}_M \ , \tag{9}$$

where $\boldsymbol{R}_f(\boldsymbol{\eta}_{\text{DMC}}) \in \mathbb{C}^{K\times K}$ is the frequency domain covariance matrix with a Toeplitz structure

$$\boldsymbol{R}_f(\boldsymbol{\eta}_{\text{DMC}}) = \text{Toep}(\boldsymbol{\kappa}(\boldsymbol{\eta}_{\text{DMC}}), \boldsymbol{\kappa}(\boldsymbol{\eta}_{\text{DMC}})^{\mathsf{H}}) \ . \tag{10}$$

In (10), $\boldsymbol{\eta}_{\text{DMC}} = [\alpha_d \ \beta_d \ \tau_d]^{\mathsf{T}}$ is the DMC parameter vector consisting of the peak power α_d, the normalized coherence bandwidth β_d and the normalized onset time τ_d, and $\boldsymbol{\kappa}(\boldsymbol{\eta}_{\text{DMC}}) \in \mathbb{C}^{K\times 1}$ represents the sampled version of the DMC power spectral density [20, Eq. (2.61)]

$$\psi_{\text{DMC}}(f) = \frac{\alpha_d}{\beta_d + j2\pi f} e^{-j2\pi f \tau_d} \ . \tag{11}$$

D. Spatial-Frequency Observations at Radio Stripes

Aggregating the received signals in (1) over K subcarriers and using the geometric model in (2) and the DMC model in (8), the spatial-frequency observation matrix at the n-th RS is

$$\begin{aligned}\boldsymbol{Y}_n &\triangleq [\boldsymbol{y}_{n,0} \ \cdots \ \boldsymbol{y}_{n,K-1}] \in \mathbb{C}^{M\times K} \\ &= \alpha_n e^{j\phi_n} \boldsymbol{a}(\theta_n)(\boldsymbol{b}(\widetilde{\tau}_n) \odot \boldsymbol{s})^{\mathsf{T}} + \boldsymbol{W}_n \ ,\end{aligned} \tag{12}$$

where $\boldsymbol{b}(\tau) \triangleq \left[1 \ e^{-j2\pi\Delta_f \tau} \ \cdots \ e^{-j2\pi(K-1)\Delta_f \tau}\right]^{\mathsf{T}} \in \mathbb{C}^{K\times 1}$ is the frequency domain steering vector, and

$$\boldsymbol{W}_n = \boldsymbol{W}_n^{\text{DMC}} \odot \mathbf{1}\boldsymbol{s}^{\mathsf{T}} + \boldsymbol{Z}_n \in \mathbb{C}^{M\times K} \tag{13}$$

represents the disturbance term consisting of the DMCs and additive white noise, with $\boldsymbol{W}_n^{\text{DMC}} = \text{reshape}_{M,K}(\boldsymbol{w}_n^{\text{DMC}}) \in \mathbb{C}^{M\times K}$ and $\boldsymbol{Z}_n = [\boldsymbol{z}_{n,0} \ \cdots \boldsymbol{z}_{n,K-1}] \in \mathbb{C}^{M\times K}$. After simple manipulations (details omitted due to lack of space), it can be shown that $\boldsymbol{W}_n$ has the distribution

$$\text{vec}\,(\boldsymbol{W}_n) \sim \mathcal{CN}(\mathbf{0}_{MK}, \boldsymbol{R}(\boldsymbol{\eta}_{\text{DMC}}, \sigma^2)) \ , \tag{14}$$

where

$$\boldsymbol{R}(\boldsymbol{\eta}_{\text{DMC}}, \sigma^2) = \left(\boldsymbol{R}_f(\boldsymbol{\eta}_{\text{DMC}}) \odot \boldsymbol{s}\boldsymbol{s}^{\mathsf{H}}\right) \otimes \mathbf{I}_M + \sigma^2 \mathbf{I}_{MK} \ . \tag{15}$$

Different methods have been proposed to estimate the DMC parameters. For instance, in [20, Sec. 6.1.8] authors provide a suitable method for finding suboptimal though accurate estimates of the DMC parameters starting from covariance matrix estimates (obtained from the observed data) and exploiting the peculiar Toeplitz structure of $\boldsymbol{R}(\boldsymbol{\eta}_{\text{DMC}}, \sigma^2)$. A similar method is adopted in [21, Sec. III-C1] to find good estimates of the DMC parameters and reconstruct an estimate of $\boldsymbol{R}(\boldsymbol{\eta}_{\text{DMC}}, \sigma^2)$. In the following, to decouple the less investigated problem of joint localization and synchronization of a UE supported by a network of RSs from the more understood problem of estimating DMC parameters, we assume that a preliminary *calibration* phase has been performed to estimate $\boldsymbol{R}(\boldsymbol{\eta}_{\text{DMC}}, \sigma^2)$, by resorting to one of the methods presented in [21], [20].

E. Problem Formulation

In the considered UL communication scenario supported by a network of RSs, our goal is to *estimate* the position of the UE and to *synchronize* its clock and phase to the RSs network. To ease the exposition and without loss of generality,we assume that the height of the UE (p_z coordinate) is assigned and the ultimate positioning problem then consists in retrieving the (p_x, p_y) coordinates, i.e., locating the UE in the $x-y$ plane.[3] Accordingly, $\boldsymbol{p}_{\text{2D}} = [p_x \ p_y]^{\mathsf{T}}$ is the 2D UE position vector.

Given the observations $\{\boldsymbol{Y}_n\}_{n=0}^{N-1}$ in (12) collected from all RSs, the problem of interest is to estimate the UE position $\boldsymbol{p}_{\text{2D}}$, its clock offset δ_τ and its phase offset δ_ϕ. The unknown parameter vector for this estimation problem is defined as

$$\boldsymbol{\eta} = [\boldsymbol{p}_{\text{2D}}^{\mathsf{T}} \ \delta_\tau \ \delta_\phi \ \overline{\boldsymbol{\alpha}}^{\mathsf{T}} \ ]^{\mathsf{T}} \in \mathbb{R}^{(N+4)\times 1} \ , \tag{16}$$

where $\overline{\boldsymbol{\alpha}} \triangleq [\alpha_0 \ \cdots \ \alpha_{N-1}]^{\mathsf{T}} \in \mathbb{R}^{N\times 1}$.

III. Joint Uplink Positioning and Synchronization

In this section, we derive novel algorithms based on the ML theory to solve the joint positioning and synchronization problem formulated in Sec. II-E.

A. Joint Direct Positioning and Synchronization

Leveraging the ML rationale, we formulate the positioning and synchronization problem as a *direct* joint estimation problem where the sought $\boldsymbol{p}_{\text{2D}}$, δ_τ, and δ_ϕ parameters are directly inferred from the raw signals collected at all RSs as

$$\widehat{\boldsymbol{\eta}}^{\text{ML}} = \arg\max_{\boldsymbol{\eta}} \ p(\{\boldsymbol{Y}_n\}_{n=0}^{N-1} \mid \boldsymbol{\eta}) \ . \tag{17}$$

Assuming independent realizations of the disturbance component $\boldsymbol{W}_n$ in (12) across the RSs, the log-likelihood version of the objective function in (17) can be written as

$$\log p(\{\boldsymbol{Y}_n\}_{n=0}^{N-1} \mid \boldsymbol{\eta}) = \sum_{n=0}^{N-1} \log p(\boldsymbol{Y}_n \mid \boldsymbol{\eta}) \ , \tag{18}$$

$$\begin{aligned}\log p(\boldsymbol{Y}_n \mid \boldsymbol{\eta}) = &-\left\| \boldsymbol{R}^{-1/2}\left[\boldsymbol{y}_n - \alpha_n e^{j\phi_n} \boldsymbol{c}(\theta_n, \widetilde{\tau}_n)\right] \right\|_2^2 \\ &- MK \log \pi - \log\det \boldsymbol{R} \ ,\end{aligned} \tag{19}$$

$\boldsymbol{c}(\theta, \tau) \triangleq (\boldsymbol{b}(\tau) \odot \boldsymbol{s}) \otimes \boldsymbol{a}(\theta) \in \mathbb{C}^{MK\times 1}$, $\boldsymbol{y}_n \triangleq \text{vec}\,(\boldsymbol{Y}_n) \in \mathbb{C}^{MK\times 1}$ and $\boldsymbol{R}$ is defined in (15) (for conciseness, we omit the dependencies on $\boldsymbol{\eta}_{\text{DMC}}$ and σ^2). Neglecting irrelevant constant terms in (18), the problem in (17) becomes

$$\widehat{\boldsymbol{\eta}}^{\text{ML}} = \arg\min_{\boldsymbol{\eta}} \ \mathcal{L}_{\text{ML}}(\boldsymbol{\eta}) \ , \tag{20}$$

where

$$\mathcal{L}_{\text{ML}}(\boldsymbol{\eta}) \triangleq \sum_{n=0}^{N-1} \left\| \boldsymbol{y}_n' - \alpha_n e^{j\phi_n} \boldsymbol{c}'(\theta_n, \widetilde{\tau}_n) \right\|_2^2 \ , \tag{21}$$

$\boldsymbol{y}_n' \triangleq \boldsymbol{R}^{-1/2}\boldsymbol{y}_n$ and $\boldsymbol{c}'(\theta, \tau) \triangleq \boldsymbol{R}^{-1/2}\boldsymbol{c}(\theta, \tau)$. To tackle ML estimation, we first notice that the amplitudes α_n in (20) can be estimated in closed-form on a per-RS basis as a function of the remaining parameters belonging to the respective RS as

$$\begin{aligned}\widehat{\alpha}_n^{\text{ML}} &= \frac{\Re\left\{(e^{j\phi_n}\boldsymbol{c}'(\theta_n, \widetilde{\tau}_n))^{\mathsf{H}}\boldsymbol{y}_n'\right\}}{\|e^{j\phi_n}\boldsymbol{c}'(\theta_n, \widetilde{\tau}_n)\|_2^2} = \frac{\Re\left\{(e^{j\phi_n}\boldsymbol{c}'(\theta_n, \widetilde{\tau}_n))^{\mathsf{H}}\boldsymbol{y}_n'\right\}}{\|\boldsymbol{c}'(\theta_n, \widetilde{\tau}_n)\|_2^2} \\ &= \frac{\left((e^{j\phi_n}\boldsymbol{c}'(\theta_n, \widetilde{\tau}_n))^{\mathsf{H}}\boldsymbol{y}_n' + (e^{j\phi_n}(\boldsymbol{y}_n')^{\mathsf{H}}\boldsymbol{c}'(\theta_n, \widetilde{\tau}_n))\right)}{2\|\boldsymbol{c}'(\theta_n, \widetilde{\tau}_n)\|_2^2}.\end{aligned} \tag{22}$$

[3] Note that the z-component of the UE position can be determined using ULAs and delay information, though with a lower accuracy due to the absence of angular elevation information. The considered scenario can be extended to provide accurate 3D localization by using 2D planar arrays in place of ULA-RSs and by including elevation angles in the estimation problem.

Plugging (22) back into (21), utilizing (3) and dropping the dependency on $\overline{\boldsymbol{\alpha}}$, we obtain the compressed log-likelihood

$$\begin{aligned}\mathcal{L}_{\text{ML}}(\boldsymbol{p}_{\text{2D}},\delta_\tau,\delta_\phi)=&\sum_{n=0}^{N-1}\Big\|\overbrace{\boldsymbol{y}'_n-\frac{(\boldsymbol{c}'(\theta_n,\widetilde{\tau}_n))^{\mathsf{H}}\boldsymbol{y}'_n}{2\left\|\boldsymbol{c}'(\theta_n,\widetilde{\tau}_n)\right\|_2^2}\boldsymbol{c}'(\theta_n,\widetilde{\tau}_n)}^{\triangleq\breve{\boldsymbol{y}}_n(\theta_n,\widetilde{\tau}_n)}\\&-\frac{e^{j2\phi_n}(\boldsymbol{y}'_n)^{\mathsf{H}}\boldsymbol{c}'(\theta_n,\widetilde{\tau}_n)}{2\left\|\boldsymbol{c}'(\theta_n,\widetilde{\tau}_n)\right\|_2^2}\boldsymbol{c}'(\theta_n,\widetilde{\tau}_n)\Big\|_2^2,\\=&\sum_{n=0}^{N-1}\left\|\breve{\boldsymbol{y}}_n(\theta_n,\widetilde{\tau}_n)-e^{j2\delta_\phi}\breve{\boldsymbol{c}}_n(\theta_n,\widetilde{\tau}_n,\tau_n)\right\|_2^2,\end{aligned}\tag{23}$$

$$\breve{\boldsymbol{c}}_n(\theta_n,\widetilde{\tau}_n,\tau_n)\triangleq\frac{e^{-j4\pi f_c\tau_n}(\boldsymbol{y}'_n)^{\mathsf{H}}\boldsymbol{c}'(\theta_n,\widetilde{\tau}_n)}{2\left\|\boldsymbol{c}'(\theta_n,\widetilde{\tau}_n)\right\|_2^2}\boldsymbol{c}'(\theta_n,\widetilde{\tau}_n)\ .\tag{24}$$

It is easy to show that also the phase offset δ_ϕ can be estimated as a function of the remaining parameters. More specifically, the δ_ϕ minimizing (23) is readily obtained as

$$\widehat{\delta}_\phi^{\text{ML}}=\frac{\angle\big(\sum_{n=0}^{N-1}\breve{\boldsymbol{c}}_n^{\mathsf{H}}(\theta_n,\widetilde{\tau}_n,\tau_n)\breve{\boldsymbol{y}}_n(\theta_n,\widetilde{\tau}_n)\big)}{2}+A\pi\ ,\tag{25}$$

where $A\in\mathbb{Z}$ is introduced to account for possible integer ambiguities in phase estimation. Inserting (25) into (23) yields

$$\begin{aligned}\mathcal{L}_{\text{ML}}(\boldsymbol{p}_{\text{2D}},\delta_\tau)=&\sum_{n=0}^{N-1}\big(\left\|\breve{\boldsymbol{y}}_n(\theta_n,\widetilde{\tau}_n)\right\|_2^2+\left\|\breve{\boldsymbol{c}}_n(\theta_n,\widetilde{\tau}_n,\tau_n)\right\|_2^2\big)\\&-2\left|\sum_{n=0}^{N-1}\breve{\boldsymbol{c}}_n^{\mathsf{H}}(\theta_n,\widetilde{\tau}_n,\tau_n)\breve{\boldsymbol{y}}_n(\theta_n,\widetilde{\tau}_n)\right|,\end{aligned}\tag{26}$$

where the direct geometric relation between the position parameters $\boldsymbol{p}=[\boldsymbol{p}_{\text{2D}}\ p_z]^{\mathsf{T}}$, δ_τ and the per-RS channel parameters $\{\theta_n,\widetilde{\tau}_n,\tau_n\}_{n=0}^{N-1}$ is specified in (4), (5), (6) and (7). The final expression of the direct ML estimator than becomes

$$[\hat{\boldsymbol{p}}_{\text{2D}}^{\text{ML}}\ \hat{\delta}_\tau^{\text{ML}}]=\arg\min_{\boldsymbol{p}_{\text{2D}},\delta_\tau}\ \mathcal{L}_{\text{ML}}(\boldsymbol{p}_{\text{2D}},\delta_\tau)\ ,\tag{27}$$

where, interestingly, the dependencies left are only upon the parameters of interest $\boldsymbol{p}_{\text{2D}}$ and δ_τ. In principle, solving (27) would require a joint optimization over the continuous support defined by the three parameters $\boldsymbol{p}_{\text{2D}}$ and δ_τ, which unfortunately is not feasible in closed-form. A more practical way to tackle (27) consists in griding the parameters support and then employing an exhaustive, but computationally demanding 3D grid search. In the following Proposition, we illustrate an alternative approach to obtain a low-complexity estimate $\hat{\delta}_\tau$.

Proposition 1. *A coarse estimate of δ_τ can be obtained by using a multilateration approach based on a low-complexity iterative least squares (ILS) procedure [26]. Specifically, by defining $\bar{\boldsymbol{Y}}_n=\text{IFFT}(\boldsymbol{Y}_n^{\mathsf{T}})$ as the IFFT-transformed observations over N_F points for each UE-RS link, we first perform a noncoherent integration across the spatial domain (i.e., samples over the M antennas at each RS) and seek for the index of the maximum element in the cost function*

$$\hat{q}=\arg\max_q\left[\sum_{m=1}^{M}|[\bar{\boldsymbol{Y}}_n]_{[q,m]}|^2:0\le q\le N_F-1\right]$$

with $|[\bar{\boldsymbol{Y}}_n]_{[q,m]}|$ denoting the absolute value of the (q,m)-th entry of $\bar{\boldsymbol{Y}}_n$. Accordingly, a coarse estimate of the pseudo-delay $\widetilde{\tau}_n$ can be obtained by mapping the index $\hat{q}$ with the corresponding IFFT bin as $\widehat{\widetilde{\tau}}_n=\hat{q}/(N_F\Delta f)$. Once the pseudo-delays $\{\widehat{\widetilde{\tau}}_n\}_{n=1}^N$ for all UE-RS links have been estimated, we can set up a system of equations expressed as a function of the parameter δ_τ (in addition to $\boldsymbol{p}$) according to (5)*. This over-determined system (for $N>3$) can be efficiently solved by adopting an ILS procedure as detailed in [27, Sec. 3.1]. We refer to the clock offset estimate as $\hat{\delta}_\tau^{ILS}$.*

The estimate $\hat{\delta}_\tau^{\text{ILS}}$ can be plugged back into (26) to reduce the optimization cost from 3D to 2D. Solving (27) for a fixed $\delta_\tau=\hat{\delta}_\tau^{\text{ILS}}$ also yields an initial estimate of $\boldsymbol{p}_{\text{2D}}$ which, given its strong dependency on the ILS estimation accuracy, will be denoted as $\hat{\boldsymbol{p}}_{\text{2D}}^{\text{ILS}}$. The ultimate ML estimates can be then obtained using a low-complexity refinement step where we solve (27) for $(\boldsymbol{p}_{\text{2D}},\delta_\tau)$ jointly by means of a low-complexity iterative optimization (e.g., Nelder-Mead algorithm), using the suboptimal estimates $\hat{\boldsymbol{p}}_{\text{2D}}^{\text{ILS}}$ and $\hat{\delta}_\tau^{\text{ILS}}$ as initialization.

B. Joint Direct Positioning and Synchronization without Exploiting Carrier Phase Information

In this section, we derive an alternative version of the direct estimator in (17) where we do not exploit the CP information in (3). Our aim is to explore the impact of phase synchronization among the RSs, represented by the parameter δ_ϕ in (17), on localization accuracy (i.e., to study if accuracy degrades when ϕ_n is assumed to be an unknown parameter that has no relation to the geometry through τ_n). In this case, by treating the channel amplitudes as unstructured complex entities $\gamma_n=\alpha_n e^{j\phi_n}\ \forall n$, the cost function in (21) becomes

$$\mathcal{L}_{\text{ML-NCP}}(\boldsymbol{\eta})\triangleq\sum_{n=0}^{N-1}\left\|\boldsymbol{y}'_n-\gamma_n\boldsymbol{c}'(\theta_n,\widetilde{\tau}_n)\right\|_2^2,\tag{28}$$

where $\gamma_n\in\mathbb{C}$, the label "ML-NCP" denotes no carrier phase (NCP), and the position-domain parameter vector becomes

$$\boldsymbol{\eta}=[\boldsymbol{p}_{\text{2D}}^{\mathsf{T}}\ \delta_\tau\ \Re\{\boldsymbol{\gamma}\}^{\mathsf{T}}\ \Im\{\boldsymbol{\gamma}\}^{\mathsf{T}}]^{\mathsf{T}}\in\mathbb{R}^{(2N+3)\times1}\ ,\tag{29}$$

with $\boldsymbol{\gamma}\triangleq[\gamma_0\ \cdots\ \gamma_{N-1}]^{\mathsf{T}}$. In (28), the estimates of the complex gains γ_n, $n=1,\dots,N$, can be obtained as

$$\widehat{\gamma}_n^{\text{ML-NCP}}=\frac{(\boldsymbol{c}'(\theta_n,\widetilde{\tau}_n))^{\mathsf{H}}\boldsymbol{y}'_n}{\left\|\boldsymbol{c}'(\theta_n,\widetilde{\tau}_n)\right\|_2^2}\ ,\tag{30}$$

leading to the compressed log-likelihood cost function

$$\mathcal{L}_{\text{ML-NCP}}(\boldsymbol{p}_{\text{2D}},\delta_\tau)=\sum_{n=0}^{N-1}\left\|\boldsymbol{\Pi}^{\perp}_{\boldsymbol{c}'(\theta_n,\widetilde{\tau}_n)}\boldsymbol{y}'_n\right\|_2^2,\tag{31}$$

where $\boldsymbol{\Pi}^{\perp}_{\boldsymbol{c}'(\theta_n,\widetilde{\tau}_n)}=\boldsymbol{I}-\frac{\boldsymbol{c}'(\theta_n,\widetilde{\tau}_n)\boldsymbol{c}'(\theta_n,\widetilde{\tau}_n)^{\mathsf{H}}}{\|\boldsymbol{c}'(\theta_n,\widetilde{\tau}_n)\|^2}$ is the orthogonal projector onto the null space spanned by $\boldsymbol{c}'(\theta_n,\widetilde{\tau}_n)$. Accordingly, the final expression of the direct ML estimator that does not exploit CP information is

$$[\hat{\boldsymbol{p}}_{\text{2D}}^{\text{ML-NCP}}\ \hat{\delta}_\tau^{\text{ML-NCP}}]=\arg\min_{\boldsymbol{p}_{\text{2D}},\delta_\tau}\ \mathcal{L}_{\text{ML-NCP}}(\boldsymbol{p}_{\text{2D}},\delta_\tau)\ .\tag{32}$$

Comparing (31) to (26), we notice in (31) the absence of a *cross-RS correlation term* represented by the last term in (26). This term links the known RSs positions and the unknown UE position through a common phase offset δ_ϕ, allowing us to exploit the CP information collectively available at all RSs to infer information about the UE location. To solve (32), we follow exactly the same rationale used for (27).

IV. Cramér-Rao Lower Bound

We adopt the theoretical tool of the CRLB to investigate the achievable accuracy of joint positioning and synchronization. The CRLB for the problem at hand is defined as [28]

$$\mathbb{E}_{\boldsymbol{\eta}}\left[(\hat{\boldsymbol{\eta}}-\boldsymbol{\eta})(\hat{\boldsymbol{\eta}}-\boldsymbol{\eta})^{\mathsf{T}}\right] \succeq \boldsymbol{J}_{\boldsymbol{\eta}}^{-1} \tag{33}$$

where $\boldsymbol{J}_{\boldsymbol{\eta}}$ is the Fisher information matrix (FIM) for the vector $\boldsymbol{\eta} = [\boldsymbol{p}_{\text{2D}}\ \boldsymbol{\delta}_{\text{c}}^{\mathsf{T}}\ \overline{\boldsymbol{\alpha}}^{\mathsf{T}}]^{\mathsf{T}}$ containing the UE position (in 2D), and nuisance parameters in form of the clock and phase synchronization parameters in $\boldsymbol{\delta}_{\text{c}}$ and the LoS amplitudes for each RS-UE link $\overline{\boldsymbol{\alpha}}$. We assume that each RS n contributes independent information on $\boldsymbol{\eta}$, i.e., assuming identical DMC and noise statistics, the FIM for the joint positioning and synchronization problem is the sum of N contributions

$$\boldsymbol{J}_{\boldsymbol{\eta}} = \sum_{n=0}^{N-1} \boldsymbol{J}_{\boldsymbol{\eta}}^{(n)} = \sum_{n=0}^{N-1} \boldsymbol{T}_n \boldsymbol{J}_{\boldsymbol{\eta}^{\text{ch}}}^{(n)} \boldsymbol{T}_n^{\mathsf{T}} \tag{34}$$

where $\boldsymbol{J}_{\boldsymbol{\eta}}^{(n)}$ represents the FIM contribution provided by the n-th RS, which are related to the channel parameter FIM $\boldsymbol{J}_{\boldsymbol{\eta}^{\text{ch}}}^{(n)}$ of each RS via the corresponding Jacobian matrix $\boldsymbol{T}_n$. The channel parameter vector of the n-th RS is defined as

$$\boldsymbol{\eta}_n^{\text{ch}} = [\theta_n\ \widetilde{\tau}_n\ \phi_n\ \alpha_n]^{\mathsf{T}} \in \mathbb{R}^{4\times 1} \tag{35}$$

containing the delay $\widetilde{\tau}_n$, the AoA θ_n, the amplitude α_n and phase ϕ_n associated to the n-th LoS path. The elements of the FIM $\boldsymbol{J}_{\boldsymbol{\eta}^{\text{ch}}}^{(n)}$ in (34) are defined as [28, Sec. 15.7]

$$[\boldsymbol{J}_{\boldsymbol{\eta}^{\text{ch}}}^{(n)}]_{i,j} = 2\Re\left\{\frac{\partial \boldsymbol{\mu}_n}{\partial [\boldsymbol{\eta}_n^{\text{ch}}]_i}^{\mathsf{H}} \boldsymbol{R}^{-1} \frac{\partial \boldsymbol{\mu}_n}{\partial [\boldsymbol{\eta}_n^{\text{ch}}]_j}\right\} \tag{36}$$

where $\boldsymbol{\mu}_n = \gamma_n \boldsymbol{c}(\theta_n, \widetilde{\tau}_n)$.

To gain insights on the achievable performance, we investigate two different scenarios: i) first, we consider the case of coherent RSs, which allows us to perform positioning by exploiting the CP, and ii) second the case of non-coherent RSs where NCP can be exploited. Due to (34), both cases can be analyzed by a suitable definition of the synchronization parameters $\boldsymbol{\delta}_{\text{c}}$ and consequently the Jacobian matrices $\boldsymbol{T}_n$

$$\boldsymbol{T}_n = \frac{\partial \boldsymbol{\eta}_n^{\text{ch}\mathsf{T}}}{\partial \boldsymbol{\eta}} = \begin{bmatrix} \boldsymbol{P}_n^{\theta} & \boldsymbol{P}_n^{\widetilde{\tau}} & \boldsymbol{P}_n^{\phi} & \boldsymbol{0} \\ \boldsymbol{0} & \boldsymbol{C}_n^{\widetilde{\tau}} & \boldsymbol{C}_n^{\phi} & \boldsymbol{0} \\ \boldsymbol{0} & \boldsymbol{0} & \boldsymbol{0} & \boldsymbol{1}_n \end{bmatrix} \in \mathbb{R}^{N+N_{\text{c}}+2\times 4}. \tag{37}$$

The block matrices relating channel parameters to the position are found as $\boldsymbol{P}^{\widetilde{\tau}} = \frac{\boldsymbol{r}_n}{c\|\boldsymbol{r}_n\|}$ from the derivative of (4) w.r.t. position and as $\boldsymbol{P}^{\phi} = \frac{-2\pi\,\boldsymbol{r}_n}{\lambda\,\|\boldsymbol{r}_n\|}$ from the derivative of (3) (inserting (4)) w.r.t. position. The selection vector $\boldsymbol{1}_n$ associates the amplitude α_n in $\boldsymbol{\eta}_n^{\text{ch}}$ with the respective amplitude in $\overline{\boldsymbol{\alpha}}$ in $\boldsymbol{\eta}$. The definition for $\boldsymbol{P}^{\theta}$ is given in Appendix A.

a) Coherent / CP: For the coherent case, the synchronization parameter vector contains clock and phase offset parameters $\boldsymbol{\delta}_{\text{c}} = [\delta_\tau\ \delta_\phi]^{\mathsf{T}}$ which are the same for all RSs, resulting in $N_{\text{c}} = 2$ synchronization parameters. The corresponding block-matrices relating the phase information of the n-th RS to phase offset and clock offset are found to be $\boldsymbol{C}^{\widetilde{\tau}} = [1\ 0]^{\mathsf{T}}$ and $\boldsymbol{C}^{\phi} = [0\ 1]^{\mathsf{T}}$.

b) Non-coherent / NCP: For the non-coherent case, the CP cannot be exploited for positioning, as each RS is assumed to have a separate phase offset $\delta_{\phi,n}$ that prevents linking the unknown UE position with the known RS positions through the phase of the received signal. The synchronization parameter vector becomes $\boldsymbol{\delta}_{\text{c}} = [\delta_\tau\ \boldsymbol{\delta}_\phi]^{\mathsf{T}}$ with $\boldsymbol{\delta}_\phi = [\delta_{\phi,1}\cdots\delta_{\phi,N}]^{\mathsf{T}}$, resulting in $N_{\text{c}} = N+1$ synchronization parameters. Consequently, one obtains a block-matrix for each phase offset parameters $\boldsymbol{C}_n^{\phi} = [0\ \boldsymbol{1}_n^{\mathsf{T}}]^{\mathsf{T}}$ as the derivatives of (3) w.r.t. the clock parameters and δ_ϕ are 1. Similarly, one obtains $\boldsymbol{C}_n^{\tau} = [1\ \boldsymbol{0}_N^{\mathsf{T}}]^{\mathsf{T}}$ for the block-matrix of the clock offset.

A. Bounds for Positioning and Synchronization

To compute the bounds for positioning and synchronization from the FIM $\boldsymbol{J}_{\boldsymbol{\eta}}$ in (34), we partition the parameter vector as $\boldsymbol{\eta} = [\boldsymbol{\eta}_{\text{w}}^{\mathsf{T}}\ \boldsymbol{\eta}_{\text{u}}^{\mathsf{T}}]^{\mathsf{T}}$, with $\boldsymbol{\eta}_{\text{w}} = [\boldsymbol{p}_{\text{2D}}\ \delta_\tau]$ containing the parameters of interest and $\boldsymbol{\eta}_{\text{u}}$ all remaining parameters as nuisance parameters [29]. Block-partitioning of the FIM

$$\boldsymbol{J}_{\boldsymbol{\eta}} = \begin{bmatrix} \boldsymbol{J}_{\boldsymbol{\eta}_{\text{w}}\boldsymbol{\eta}_{\text{w}}} & \boldsymbol{J}_{\boldsymbol{\eta}_{\text{w}}\boldsymbol{\eta}_{\text{u}}} \\ \boldsymbol{J}_{\boldsymbol{\eta}_{\text{w}}\boldsymbol{\eta}_{\text{u}}}^{\mathsf{T}} & \boldsymbol{J}_{\boldsymbol{\eta}_{\text{u}}\boldsymbol{\eta}_{\text{u}}} \end{bmatrix} \in \mathbb{R}^{(N+N_{\text{c}}+2)\times(N+N_{\text{c}}+2)} \tag{38}$$

allows to make use of the notion of the equivalent FIM (EFIM) [30], [31] to obtain $\boldsymbol{J}_{\text{e}} = \boldsymbol{J}_{\boldsymbol{\eta}_{\text{w}}\boldsymbol{\eta}_{\text{w}}} - \boldsymbol{J}_{\boldsymbol{\eta}_{\text{w}}\boldsymbol{\eta}_{\text{u}}} \boldsymbol{J}_{\boldsymbol{\eta}_{\text{u}}\boldsymbol{\eta}_{\text{u}}}^{-1} \boldsymbol{J}_{\boldsymbol{\eta}_{\text{w}}\boldsymbol{\eta}_{\text{u}}}^{\mathsf{T}} \in \mathbb{R}^{3\times 3}$ [29], relating to CRLB for position and clock offset via (33). The position error bound (PEB) and clock error bound (CEB) are then defined as

$$\mathcal{P} = \sqrt{\text{tr}\{[\boldsymbol{J}_{\text{e}}^{-1}]_{1:2,1:2}\}}, \qquad \mathcal{C}_\tau = \sqrt{[\boldsymbol{J}_{\text{e}}^{-1}]_{3,3}}. \tag{39}$$

V. Simulation Results

We conduct simulation campaigns to assess the actual estimation performance provided by the novel ML-based estimators, also in comparison with the theoretical lower bounds.

A. Scenario

The considered scenario consists of a network of $N = 4$ RSs deployed over an area of $(10\times 10)\,\text{m}^2$ placed at the height of $5\,\text{m}$ from the floor, and of a single UE located at $\boldsymbol{p} = [7\ 3\ 1]^{\mathsf{T}}$. The RSs are distributed on each corner so as to provide uniform coverage. Each RS is equipped with a ULA with $M = 4$ antennas spaced at $d = \lambda/2$. The UE transmits OFDM signals in the uplink channel at a carrier frequency $f_c = 3.5\,\text{GHz}$, with a bandwidth $B = 100\,\text{MHz}$, over $K = 100$ subcarriers. For these parameters, the near-field region extends to about 2.3 km from the UE position (Fraunhofer distance $d_F = 2D^2/\lambda$, with $D = 10$ m). We set the UE clock and phase offsets to $\delta_\tau = 100/c\,\text{s}$ and $\delta_\phi = 10\,\text{deg}$, respectively. The channel amplitudes are generated as $\alpha_n = \sqrt{P}\rho_n$ where P is the UE transmit power and ρ_n is set according to the free space path loss model, i.e., $\rho_n = \lambda/(4\pi\|\boldsymbol{p} - \boldsymbol{p}_n^{\text{RS}}\|)$, whereas the noise power is $\sigma^2 = k_B T_0 B$, k_B being the Boltzmann constant and T_0 the standard thermal noise temperature. As to the DMC, we set the normalized coherence bandwidth $\beta_d = 1/(T_d B)$ with $T_d = 20/c$ decay time set to a distance of $20\,\text{m}$, the normalized onset time to $\tau_d = \frac{B}{K}(\tau_n + 1\,\text{m}/c)$, i.e., the DMC onset is delayed by $1\,\text{m}$ w.r.t. the LoS, and the peak power α_d is chosen to guarantee a dense-multipath-to-noise ratio (DNR), defined as $\text{DNR} = \alpha_d/\sigma^2$, equal to $20\,\text{dB}$. To quantify the average signal power received by the whole RS network, we define an average SDNR as[4]

$$\overline{\text{SDNR}} = \frac{P}{NK}\sum_{n=0}^{N-1} \rho_n^2\ \boldsymbol{c}^{\mathsf{H}} \boldsymbol{R}_n^{-1} \boldsymbol{c} \tag{40}$$

[4]This definition should be seen as a positioning-specific metric, being the DMC contributions treated as disturbance terms. Conversely, for communication-oriented tasks, DMC can be included in the useful signal part.

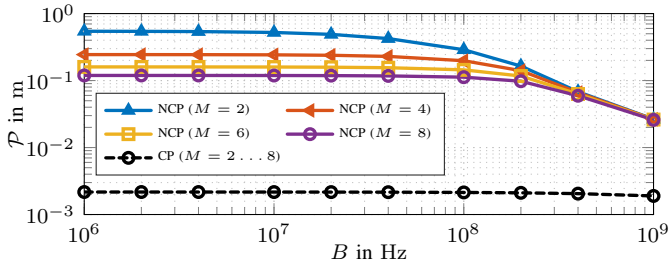

Fig. 2. PEB as a function of the bandwidth B for different number of antennas M. The comparison includes RSs either exploiting carrier-phase (CP) information or ignoring it (NCP), at a fixed $\overline{\text{SDNR}} \approx 12\,\text{dB}$.

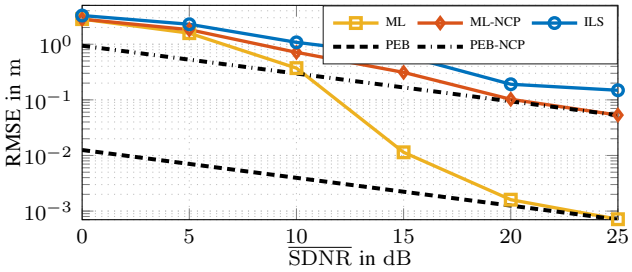

Fig. 3. RMSE on UE position estimation compared to PEB as a function of the $\overline{\text{SDNR}}$, either exploiting CP or ignoring it (NCP).

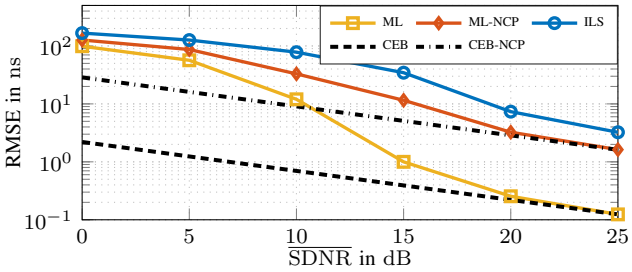

Fig. 4. RMSE on clock-offset estimation compared to CEB as a function of the $\overline{\text{SDNR}}$, either exploiting CP or ignoring it (NCP).

where index n is added to $\boldsymbol{R}$ to make explicit that also the DMC power will vary between RSs, in realistic scenarios.

B. Analysis of the Positioning Bounds

We start by analyzing the PEBs derived in Sec. IV to investigate how the number of antennas M per RS and bandwidth B impact on the ultimate positioning accuracy. Fig. 2 shows these bounds evaluated for both positioning with carrier-phase (CP) and without (NCP). During the analysis, we keep a constant $\overline{\text{SDNR}} \approx 12\,\text{dB}$, which cancels the effect of a varying array gain when varying M. The first important fact can be highlighted by comparing the curves corresponding to the two groups of PEBs: the evident gap between the case in which CP information is exploited, and the case where it is not, clearly demonstrates the crucial role that such information has on the positioning accuracy. As a matter of fact, exploiting CP information brings about two orders of magnitude improvements in the ultimate UE localization accuracy, with errors that can be as low as a few millimeters. Delving into more specific details, in the NCP case we observe that the array aperture, i.e., its angular resolution, dominates the PEB for low bandwidths. For high bandwidths, the PEB is instead dominated by its high time resolution. In the CP case, interestingly, varying the number of antennas or bandwidth has a negligible impact on the PEB. This behavior is linked to the fact that the accuracy from phase-aided positioning exploiting the fully coherent RS infrastructure dominates over both its time and angular resolutions. The likelihood function underlying the CP-based positioning exhibits very sharp peaks at the spatial intersections of the wavefronts associated to each RS. The very informative peak around the true position $\boldsymbol{p}_{\text{2D}}$, however, comes at the price of a multimodal likelihood function, and thus a computationally more demanding estimation problem. More quantitatively, resolution of (27) involves a cost about 38% higher than the cost needed to solve (32).

C. Algorithms Performance Assessment

We now assess the performance of the ML-based estimation algorithms developed in Sec. III. In Fig. 3, we report the root-mean-squared error (RMSE) on the estimation of the UE position $\boldsymbol{p}_{\text{2D}}$, obtained by averaging the results over 1000 independent Monte Carlo trials, as a function of the $\overline{\text{SDNR}}$. The comparison includes the ML algorithm that exploits the CP information, its relaxed version ML-NCP that ignores the existence of a relationship between the phase of the signal received at each RS and the unknown UE position, and the theoretical lower bounds derived in Sec. IV acting as *benchmark*. For completeness, we also report the performance of the ILS estimator which is used to obtain an initial estimate of both UE position and synchronization offset.

From an algorithmic perspective, it can be noticed that all the approaches start by exhibiting quite high RMSEs for low values of the $\overline{\text{SDNR}}$. This behavior can be explained by observing that the suboptimal ILS approach that is used to initialize the ML estimators is not very accurate in such a regime. However, as soon as the initialization provided by the ILS improves, the RMSEs of the ML estimators immediately drop and tend to approach the corresponding lower bounds. Remarkably, the proposed ML estimator that exploits CP information achieves an accuracy in the order of about $1\,\text{cm}$ for $\overline{\text{SDNR}} = 15\,\text{dB}$, and further enhances until mm-level accuracy as the $\overline{\text{SDNR}}$ increases. A similar trend is observed in the RMSE of the ML-NCP, which however requires a $\overline{\text{SDNR}}$ of about $20\,\text{dB}$ to attain values in the order of $10\,\text{cm}$.

To complement the above analysis, in Fig. 4 we evaluate the performance on the estimation of the UE clock offset δ_τ (similar results are obtained also for the phase offset δ_ϕ, hence they are omitted). A direct comparison of the CEBs confirms that the use of CP information has a beneficial effect also on the synchronization accuracy, with improvements of about one order of magnitude compared to the case in which such information is not exploited. Consistently with the results in Fig. 3, also in this case the algorithms exhibit higher RMSE values in the lower $\overline{\text{SDNR}}$ regime, due to the poor accuracy of the initialization provided by the ILS algorithm. Interestingly, the proposed ML estimator that leverages CP information guarantees an accurate synchronization in the order of $1\,\text{ns}$ already for $\overline{\text{SDNR}} \geq 15\,\text{dB}$, significantly outperforming the ML-NCP algorithm that instead needs about $10\,\text{dB}$ more to achieve a comparable level of accuracy.

VI. Conclusion

We addressed the problem of accurate positioning exploiting coherent processing performed by distributed RSs, a promising technology for future wireless networks. To take advantage of the large aperture achieved by the spatial distribution of the RSs, accurate time- and phase- synchronization need to be recovered. To this aim, we proposed a novel ML algorithm that jointly estimates the synchronization parameters alongside the UE position, for a propagation scenario consisting of an LoS-path plus DMC modeling disturbance from diffuse multipath. Two variants of the ML estimator were derived, assuming either a fully coherent or a non-coherent RS network. Results show that the coherent ML algorithm significantly outperforms its non-coherent counterpart. Moreover, use of CP enables high accuracy positioning even with fewer per-RS antenna elements, as the position-related information in the CP is rich and compensates for the reduced aperture.

Appendix A
Jacobian Matrix: Block Matrix for AoA

To obtain $\boldsymbol{P}^{\theta}$ we denote the vector from the n-th RS to the UE as $\boldsymbol{r}_n = [r_{xn}\ r_{yn}]^{\mathsf{T}}$ with $r_{xn} = p_x - x_n^{\mathrm{RS}}$ and $r_{yn} = p_y - y_n^{\mathrm{RS}}$. For RSs horizontally non-colocated with the UE, i.e., $\boldsymbol{r}_n \neq \boldsymbol{0}$, one obtains

$$\boldsymbol{P}^{\theta} = \begin{cases} \begin{bmatrix} \frac{r_{yn}}{r_{xn}^2+r_{yn}^2} & \frac{-r_{xn}}{r_{xn}^2+r_{yn}^2} \end{bmatrix}^{\mathsf{T}}, & [\boldsymbol{p}_n']_1 \neq 0 \\ \boldsymbol{0}\,, & [\boldsymbol{p}_n']_1 = 0, [\boldsymbol{p}_n']_2 \neq 0 \end{cases} \tag{41}$$

through the position-related derivatives of (6).

Appendix B
Fisher Information Matrix

The elements of the FIM $\boldsymbol{J}_{\boldsymbol{\eta}^{\mathrm{ch}}}$ in (36) are given below, omitting the index n for brevity. Due to symmetry, $[\boldsymbol{J}_{\boldsymbol{\eta}^{\mathrm{ch}}}]_{j,i} = [\boldsymbol{J}_{\boldsymbol{\eta}^{\mathrm{ch}}}]_{i,j}$ holds and the FIM is described through its elements

$$\begin{aligned}
&\boldsymbol{J}_{\theta,\theta} = 2\Re\left\{\alpha_n^2 \dot{\boldsymbol{c}}_{\theta}^{\mathsf{H}} \boldsymbol{R}^{-1} \dot{\boldsymbol{c}}_{\theta}\right\} && \boldsymbol{J}_{\theta,\tilde{\tau}} = 0 \\
&\boldsymbol{J}_{\theta,\phi} = 0 && \boldsymbol{J}_{\theta,\alpha} = 0 \\
&\boldsymbol{J}_{\tilde{\tau},\tilde{\tau}} = 2\Re\left\{\alpha_n^2 \dot{\boldsymbol{c}}_{\tilde{\tau}}^{\mathsf{H}} \boldsymbol{R}^{-1} \dot{\boldsymbol{c}}_{\tilde{\tau}}\right\} && \boldsymbol{J}_{\tilde{\tau},\phi} = 2\Re\left\{j\alpha_n^2 \dot{\boldsymbol{c}}_{\tilde{\tau}}^{\mathsf{H}} \boldsymbol{R}^{-1} \boldsymbol{c}\right\} \\
&\boldsymbol{J}_{\tilde{\tau},\alpha} = 2\Re\left\{\alpha_n \dot{\boldsymbol{c}}_{\tilde{\tau}}^{\mathsf{H}} \boldsymbol{R}^{-1} \boldsymbol{c}\right\} && \boldsymbol{J}_{\phi,\phi} = 2\Re\left\{\alpha_n^2 \boldsymbol{c}^{\mathsf{H}} \boldsymbol{R}^{-1} \boldsymbol{c}\right\} \\
&\boldsymbol{J}_{\phi,\alpha} = 0 && \boldsymbol{J}_{\alpha,\alpha} = 2\Re\left\{\boldsymbol{c}^{\mathsf{H}} \boldsymbol{R}^{-1} \boldsymbol{c}\right\}
\end{aligned}$$

with $\boldsymbol{c} = (\boldsymbol{b} \odot \boldsymbol{s}) \otimes \boldsymbol{a}$, $\dot{\boldsymbol{c}}_{\theta} = \frac{\partial \boldsymbol{c}}{\partial \theta} = (\boldsymbol{b} \odot \boldsymbol{s}) \otimes \dot{\boldsymbol{a}}$ and $\dot{\boldsymbol{c}}_{\tilde{\tau}} = \frac{\partial \boldsymbol{c}}{\partial \tilde{\tau}} = (\dot{\boldsymbol{b}} \odot \boldsymbol{s}) \otimes \boldsymbol{a}$. Notice that due to the selection of the array reference point, the elements $\boldsymbol{J}_{\theta,\tilde{\tau}}$, $\boldsymbol{J}_{\theta,\phi}$ and $\boldsymbol{J}_{\theta,\alpha}$ vanish.

Acknowledgments

This work was supported, in part, by the Swedish Research Council project 2022-03007, and in part by the European Union's Horizon 2020 research and innovation programme under grant agreement No 101013425 (Project "REINDEER").

References

[1] E. Nayebi *et al.*, "Cell-free massive MIMO systems," in *2015 49th Asilomar Conf. on Sign., Syst. and Comp.*, 2015, pp. 695–699.
[2] Ö. T. Demir *et al.*, "Foundations of user-centric cell-free massive MIMO," *Foundations and Trends® in Signal Processing*, vol. 14, no. 3-4, pp. 162–472, 2021.
[3] G. Interdonato *et al.*, "Ubiquitous cell-free massive MIMO communications," *EURASIP Journal on Wireless Communications and Networking*, vol. 2019, no. 1, pp. 1–13, 2019.
[4] A. Sakhnini *et al.*, "Near-field coherent radar sensing using a massive MIMO communication testbed," *IEEE Transactions on Wireless Communications*, vol. 21, no. 8, pp. 6256–6270, 2022.
[5] ——, "An experimental evaluation of robust near-field radar localization using a massive MIMO testbed," in *2022 2nd IEEE International Symposium on Joint Communications and Sensing (JCS)*, 2022, pp. 1–6.
[6] F. Liu *et al.*, "Integrated sensing and communications: Toward dual-functional wireless networks for 6G and beyond," *IEEE Journal on Selected Areas in Communications*, vol. 40, no. 6, pp. 1728–1767, 2022.
[7] A. M. Haimovich *et al.*, "MIMO radar with widely separated antennas," *IEEE Signal Processing Magazine*, vol. 25, no. 1, pp. 116–129, 2008.
[8] Z. H. Shaik *et al.*, "MMSE-optimal sequential processing for cell-free massive MIMO with radio stripes," *IEEE Transactions on Communications*, vol. 69, no. 11, pp. 7775–7789, 2021.
[9] U. K. Ganesan *et al.*, "BeamSync: Over-the-air carrier synchronization in distributed RadioWeaves," in *WSA 2021; 25th International ITG Workshop on Smart Antennas*, 2021, pp. 1–6.
[10] B. J. Deutschmann *et al.*, "Location-based initial access for wireless power transfer with physically large arrays," *arXiv preprint arXiv:2202.10749*, 2022.
[11] U. K. Ganesan *et al.*, "RadioWeaves for extreme spatial multiplexing in indoor environments," in *2020 54th Asilomar Conference on Signals, Systems, and Computers*, 2020, pp. 1007–1011.
[12] D. Dardari *et al.*, "LOS/NLOS near-field localization with a large reconfigurable intelligent surface," *IEEE Transactions on Wireless Communications*, vol. 21, no. 6, pp. 4282–4294, 2022.
[13] N. BniLam *et al.*, "Synchronization of multiple independent subarray antennas: An application for angle of arrival estimation," *IEEE Trans. on Antennas and Propagation*, vol. 67, no. 2, pp. 1223–1232, 2019.
[14] A. K. Mishra *et al.*, "Millimeter wave and radio stripe: A prospective wireless technology for 6G and beyond networks," in *2021 Smart Technologies, Communication and Robotics (STCR)*, 2021, pp. 1–3.
[15] O. L. A. López *et al.*, "Massive MIMO with radio stripes for indoor wireless energy transfer," *IEEE Trans. on Wirel. Comm.*, pp. 1–1, 2022.
[16] N. Vukmirović *et al.*, "Direct wideband coherent localization by distributed antenna arrays," *Sensors*, vol. 19, no. 20, p. 4582, 2019.
[17] ——, "Position estimation with a millimeter-wave massive MIMO system based on distributed steerable phased antenna arrays," *EURASIP journal on advances in signal processing*, vol. 2018, pp. 1–17, 2018.
[18] ——, "Performance limits of direct wideband coherent 3D localization in distributed massive mimo systems," *Sensors*, vol. 21, no. 10, 2021.
[19] M. E. Leinonen *et al.*, "Initial radio models and analysis towards ultra-high data rate links in 6G," Hexa-X project Deliverable D2.2, 2021. [Online]. Available: https://hexa-x.eu/deliverables/
[20] A. Richter, "Estimation of radio channel parameters: Models and algorithms." ISLE Blacksburg, VA, USA, 2005.
[21] X. Li *et al.*, "Massive MIMO-based localization and mapping exploiting phase information of multipath components," *IEEE Transactions on Wireless Communications*, vol. 18, no. 9, pp. 4254–4267, 2019.
[22] O. Edfors *et al.*, "Initial assessment of architectures and hardware resources for a RadioWeaves infrastructure," Jan. 2022. [Online]. Available: https://doi.org/10.5281/zenodo.5938909
[23] "Discussion of potential techniques for NR positioning," in *CATT, 3GPP R1-1810532*, 2018.
[24] B. Behmanesh *et al.*, "Analytical performance metrics and physical-layer solutions," Jan. 2022. [Online]. Available: https://doi.org/10.5281/zenodo.5938647
[25] E. Tanghe *et al.*, "Experimental analysis of dense multipath components in an industrial environment," *IEEE Transactions on Antennas and Propagation*, vol. 62, no. 7, pp. 3797–3805, 2014.
[26] J. Yan *et al.*, "A framework for low complexity least-squares localization with high accuracy," *IEEE Transactions on Signal Processing*, vol. 58, no. 9, pp. 4836–4847, 2010.
[27] A. Coluccia *et al.*, "Hybrid TOA/RSS range-based localization with self-calibration in asynchronous wireless networks," *Journal of Sensor and Actuator Networks*, vol. 8, no. 2, 2019.
[28] S. M. Kay, *Fundamentals of Statistical Signal Processing: Estimation Theory*. Upper Saddle River, NJ: Prentice Hall, 1993.
[29] H. L. Van Trees, *Optimum Array Processing: Part IV of Detection, Estimation, and Modulation Theory*, ser. Detection, Estimation, and Modulation Theory. John Wiley & Sons, Inc., 2002.
[30] Y. Shen *et al.*, "Fundamental limits of wideband localization - part i: A general framework," *IEEE Transactions on Information Theory*, vol. 56, no. 10, pp. 4956–4980, 2010.
[31] Y. Han *et al.*, "Performance limits and geometric properties of array localization," *IEEE Transactions on Information Theory*, vol. 62, no. 2, pp. 1054–1075, 2016.